ACS Sustainable Chemistry & Engineering

pubs.acs.org/journal/ascecg

Research Article

Novel Phosphorus-Doped Magnetic and Deactivation-Resistant Solid Catalysts for Nonenzymatic Sugar Production from Biomass Hemicellulose

Yiping Luo, Bin Jiang, Javier Remón, Jie Wu, Xiaoyu Zhu, Fang Deng, Hongquan Fu, Tianjie Ao,* and Dong Li

Cite This: https://doi.org/10.1021/acssuschemeng.5c11136

ABSTRACT: The development of a cost-effective process for biomass conversion into sugar platforms is a cornerstone of sustainable biorefining. Here, we report a Lewis acid-controlled catalytic strategy for nonenzymatic sugar production from hemicellulose in biomass using a highly active, magnetically separable core−shell catalyst. The catalyst comprises a Fe_3O_4 magnetic core, an acid-resistant silica interlayer, and a phosphorus (P)-doped porous carbon shell. Under mild hydrothermal conditions, the optimized catalyst ($MC_{600}P_{1.2}$) achieved a xylose yield of 86.9% from xylan (100 °C for 2 h) and 60.3−91.0% from diverse biomass feedstocks (corncob, corn stover, poplar, and bamboo, 160 °C for 2 h), outperforming previously reported systems. Such remarkable catalytic activity is attributed to the unique structural design of the catalyst. The silica interlayer acts as a protective shield of Fe_3O_4 core and bonds with the carbon layer to form a silica−carbon shell that provides an ideal scaffold. Meanwhile, P doping introduces defects and hydrogen bonds, enhancing the active site accessibility. The formation of thermally stable PO_x species (C−P−O, C_3−P═O, and C−O−P) on the carbon support acts as Lewis acid sites. C−P−O efficiently activates H_2O to produce H^+ for glycosidic bond cleavage and suppresses xylose degradation, ensuring a high yield. These features result in high catalytic stability and reusability, maintaining high xylose yields after three consecutive cycles. This work provides new research avenues to produce nonenzymatic sugar based on active, deactivation-resistant, and easily recoverable heterogeneous catalysts.

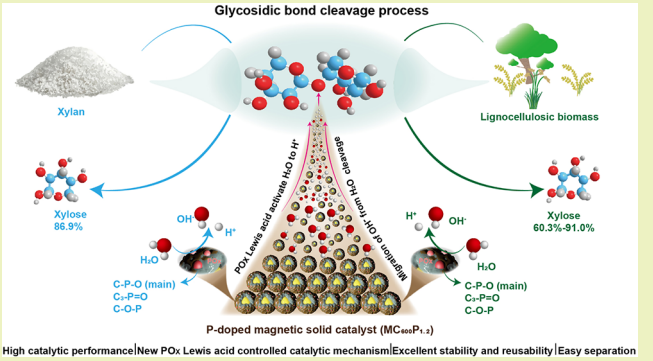

KEYWORDS: *hemicellulose valorization, nonenzymatic sugar production, phosphorus-doped magnetic solid catalyst, Lewis acid catalytic strategy, sustainable biorefining*

INTRODUCTION

The increasing severity of environmental issues and dwindling resources is largely attributed to the heavy dependence of humans on fossil fuels, highlighting the need for a transition to renewable resources.[1] Lignocellulosic biomass, with a worldwide annual output of about 200 billion metric tons, stands as a renewable and abundant source for producing value-added chemicals.[2,3] The "similarity principle", taking into account the inherent chemical structures and functionalities of components to maintain high atom efficiency, reveals significant promise for biomass maximum utilization.[4] This latter is vital for the sustainable utilization of carbohydrate fractions (hemicellulose and cellulose), as these account for 60−80% of lignocellulosic biomass. Following cost-effective strategies allows for the conversion of carbohydrates into sugar platform molecules, preserving their native structures and thus avoiding degradation and subsequent formation pathways that reduce atom efficiency. Such platform molecules are paramount, as they can be used as building blocks to produce chemicals, fuels, and polymeric materials.[5]

Enzymatic hydrolysis is widely used for converting biomass carbohydrates into sugars, owing to its superior product selectivity and eco-friendly nature.[6] However, it faces several challenges, such as the high cost of commercial enzymes, nonproductive binding of cellulase to lignin, enzyme inhibition, and slow reaction rates.[7,8] Additionally, pretreatment technologies are considered an essential step prior to enzymatic hydrolysis to reduce the recalcitrance of biomass and enhance enzyme accessibility. These pretreatment processes help

Received: October 15, 2025
Revised: December 2, 2025
Accepted: December 3, 2025

partially or entirely remove hemicellulose and/or lignin, thereby enhancing the enzymatic saccharification of cellulose.[9] However, such tandem processes result in inefficient utilization of hemicellulose (primarily composed of C5 sugars such as xylose), as it is removed as waste or nonspecifically converted during pretreatment, leading to actual sugar yields that fall short of theoretical expectations. Therefore, it is essential to develop novel, cost-effective methods to produce C5 sugar platforms (primarily xylose) from hemicellulose in biomass.

Taking these considerations into account, acid hydrolysis stands as an effective technique to produce xylose by cleaving glycosidic bonds from hemicellulose in biomass.[10] While efficient, it suffers from several catalytic issues when homogeneous liquid catalysts are used, i.e., the corrosive nature of the mineral acids used as catalysts, and the challenging separation and recovery of these liquids from the reaction medium.[11] Alternatively, heterogeneous solid acids are gaining popularity for their effectiveness, environmental benefits, and easy separation from the liquid reaction products.[12] Notably, sulfonated carbon-based solid acids stand out as promising and cost-effective catalysts for biomass saccharification. This is accounted for by their acidic functional groups, such as $-SO_3H$, $-COOH$, and $-OH$, which effectively attack the β-1,4-glycosidic bonds, promoting the hydrolysis of hemicellulose into xylose.[13] Despite these catalysts being easily recovered from the aqueous reaction medium, their separation from the residual solid biomass remains challenging.

To tackle this issue, magnetic solid acid catalysts offer a promising solution, enabling easy separation from both liquid and solid phases. Research in this area has mainly focused on magnetic Brønsted solid acids, such as sulfonated mesoporous silica and amorphous carbon, which have shown excellent performance in biomass hydrolysis owing to their abundant acid sites and uniform channels that allow reactants to access these sites efficiently.[14,15] Qi et al. developed a sulfonated magnetic carbon-based solid acid (MMCSA) for corncob saccharification, achieving 74.9% xylose yield in water at 150 °C for 2 h.[16] However, the inevitable leaching of $-SO_3H$ groups from catalysts decreased the catalytic activity, limiting its industrial applications. Therefore, the development of effective, deactivation-resistant magnetic solid catalysts could unlock promising opportunities for hemicellulose saccharification.

On this matter, phosphorus (P)-doped carbon materials have made important progress in the field of catalysis.[17,18] This results from P, with its relatively low electronegativity (2.19) and large atomic radius (1.06 Å), effectively enhancing electron transfer and increasing defect sites in carbon materials.[19] Notably, P doping alters chemical bonds, leading to modifications in the charge distribution around neighboring atoms, thus improving catalytic kinetics on the surface of the material.[20] Cao et al. demonstrated that P-doped biochar exhibited outstanding catalytic activity for rice starch hydrolysis, achieving 86.5% glucose at 150 °C for 20 min.[17] This high catalytic activity was primarily due to the formation of acidic $C-O-PO_3$ and $C-PO_3$ groups. Despite these excellent prospects, no studies have reported the use of P-doped magnetic solid catalysts for hemicellulose saccharification. Furthermore, a deeper understanding of the catalytic mechanism of the formed P-containing species for hemicellulose saccharification is needed to design more efficient catalysts to advance this research.

Given this background and research gap, this work reports, for the first time, the development of a Lewis acid-controlled catalytic strategy for nonenzymatic sugar production from biomass hemicellulose using P-doped, magnetic core−shell solid catalysts. Our novel catalyst included a magnetic Fe_3O_4 core encapsulated with a P-doped silica−carbon shell, synthesized through high-temperature carbonization. The unique design of the catalyst prevented its agglomeration while preserving good magnetism for easy separation. The catalyst's activity, stability, and reusability in the conversion of hemicellulose from various biomass substrates into xylose were evaluated. Additionally, an in-depth investigation of the potential catalytic mechanisms involving P-containing species on the magnetic solid catalyst for hemicellulose saccharification was conducted, providing new insights into sustainable sugar platform production with new engineering applications. As a result, this work paves the way for the commercial application of novel, highly recoverable, and deactivation-resistant phosphorus-doped magnetic carbon-based catalysts for sustainable biorefining.

EXPERIMENTAL SECTION

Materials. Xylan (RG, >85%, Adamas), tetraethyl orthosilicate (TEOS, AR, $SiO_2 \geq 28.4\%$, Greagent), microcrystalline cellulose (MC, RG, Adamas), iron chloride ($FeCl_3$, AR, 98%, Adamas), ferrous sulfate ($FeSO_4 \bullet 7H_2O$, AR, ≥99.0%, Greagent), and phosphoric acid (H_3PO_4, AR, ≥85%, Chengdu Colon Chemical Co., LTD) were obtained from commercial suppliers and used as received. Corncob (Yuanping City, Shanxi Province, China), corn stover (Chengdu City, Sichuan Province, China), poplar (Heze City, Shandong Province, China), and bamboo (Lishui City, Zhejiang Province, China) were finely ground and screened to achieve a particle size of 20−40 mesh before use. The contents of hemicellulose, cellulose, and lignin in these four types of biomass are provided in Table S1.

Preparation of P-Doped Magnetic Solid Catalysts. Fe_3O_4 magnetic particles were synthesized using the coprecipitation method by mixing $FeCl_3$ and $FeSO_4 \cdot 7H_2O$ in a molar ratio of 2:1 (Fe^{3+} to Fe^{2+}), with $NH_3 \bullet H_2O$ (25 wt %) being added gradually. Subsequently, a silica layer was coated onto 4 g of the as-synthesized Fe_3O_4 particles using the sol−gel method, in which 20 mL of TEOS was added gradually. The resulting solid product was designated as $Fe_3O_4@SiO_2$. To form a carbon layer on $Fe_3O_4@SiO_2$, 4 g of $Fe_3O_4@SiO_2$ and 1.6 g of MC, serving as the precursor and carbon source, respectively, were mixed in 50 mL of ethanol/H_2O (1:1, v/v) solution and aged at 180 °C for 10 h. The obtained solid was labeled as $Fe_3O_4@SiC$. For P doping, 1 g of $Fe_3O_4@SiC$ was first immersed in a certain volume of H_3PO_4 (0.3−1.4 mL) solution for 24 h, then dried at 105 °C to obtain P-enriched $Fe_3O_4@SiC$. They were further carbonized under different temperatures (300−700 °C) for 2 h and different times (0.5−4 h) at 600 °C, with a heating rate of 5 °C/min and an N_2 flow rate of 60 mL/min. The obtained P-doped magnetic solid catalysts were denoted as MC_xP_y. Here, x represents the activation temperature (°C), and y (mL/g) denotes the volume/mass ratio of H_3PO_4 (mL) to $Fe_3O_4@SiC$ (g).

For comparison, P-enriched $Fe_3O_4@SiO_2$ was prepared using a similar procedure, with a H_3PO_4 dosage of 1 mL/g. The $Fe_3O_4@SiO_2$, $Fe_3O_4@SiC$, and P-enriched $Fe_3O_4@SiO_2$ samples were then carbonized at 600 °C for 2 h under a N_2 atmosphere, producing solid samples labeled MSi (silica-coated Fe_3O_4), MC (silica−carbon-coated Fe_3O_4), and MSiP (P-doped MSi), respectively. Additional details of P-doped magnetic solid catalyst preparation are available in the Supporting Information.

Catalytic Saccharification of Hemicellulose in Biomass. Xylan, a representative of hemicellulose in biomass, was utilized to produce xylose via a hydrothermal catalytic method with MC_xP_y. In this procedure, 0.1 g of xylan, 0.02−0.14 g of MC_xP_y, and 20 mL of H_2O were added into a sealed autoclave (Beijing Century Senlong

https://doi.org/10.1021/acssuschemeng.5c11136
ACS Sustainable Chem. Eng. XXXX, XXX, XXX−XXX

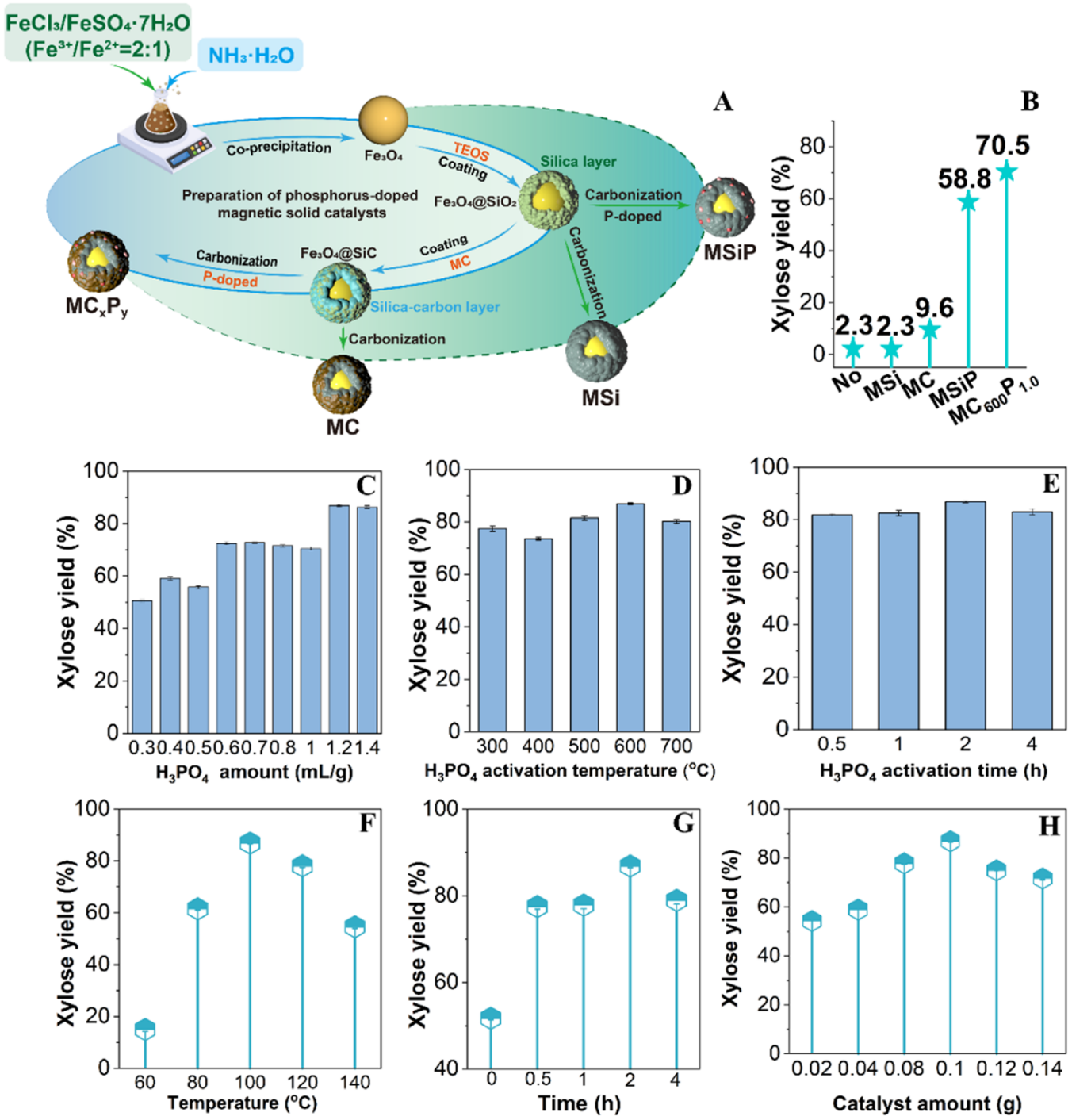

Figure 1. (A) Images of various core−shell magnetic solid catalysts and (B) the corresponding catalytic activities for xylan hydrolysis at 100 °C for 2 h; (C−E) optimization of catalyst preparation conditions, including H_3PO_4 amount ($MC_{600}P_{0.3-1.4}$, 2 h), activation temperature ($MC_{300-700}P_{1.2}$, 2 h), and activation time ($MC_{600}P_{1.2}$, 600 °C) for xylan hydrolysis at 100 °C; (F−H) optimization of reaction temperature (0.1 g $MC_{600}P_{1.2}$, 2 h), reaction time (0.1 g $MC_{600}P_{1.2}$, 100 °C), and catalyst amount (0.02−0.14 g $MC_{600}P_{1.2}$, 100 °C, 2 h) for xylan hydrolysis.

Experimental Apparatus Co., Ltd.). Prior to the addition of 1.0 MPa of N_2 at the beginning, the inner air of the autoclave was purged with N_2 for 2 min. When the reactor attained the target temperature, the reaction time was measured. Once the reaction was completed and the reactor cooled, the mixture containing a liquid solution and solid samples was obtained. Following the reaction, xylan dissolved entirely, permitting the direct separation of solid MC_xP_y by using an external magnet. This catalyst was collected for further study. The liquid solution was then analyzed to determine various product yields. Various magnetic solid catalysts were also tested for their catalytic performance using a similar method.

The catalytic hydrothermal conversion of various biomasses, including corncob, corn stover, poplar, and bamboo, was carried out in water using the optimized MC_xP_y formulation. Typically, 0.5 g of biomass, 0.5 g of MC_xP_y, and 50 mL of H_2O were added into a sealed autoclave. The reaction condition was 160 °C for 2 h. When the reaction finished, the mixture was filtered to separate the solid products from the liquid. The dried solids were then subjected to magnetic separation to recover MC_xP_y.

https://doi.org/10.1021/acssuschemeng.5c11136
ACS Sustainable Chem. Eng. XXXX, XXX, XXX−XXX

Catalyst Reusability. The catalyst reusability was assessed following the same procedure as described above procedure. Each catalytic cycle was designated as MC_xP_y-m (m), where m indicates the cycle number. To improve the catalytic efficiency of the used MC_xP_y, two methods were employed as follows. In the first strategy, MC_xP_y-m was washed with water three times and dried at 105 °C, with the resulting catalyst named MC_xP_y-W_m (W_m) for future applications. In the second strategy, MC_xP_y-m was subjected to carbonization at 600 °C for 2 h under a N_2 atmosphere, and the regenerated catalyst was named MC_xP_y-R_m (R_m) for utilization in the subsequent cycle.

Catalyst Characterization. The surface morphologies of the catalysts were assessed by using scanning electron microscopy (SEM, ZEISS Sigma 300, Germany) and transmission electron microscopy (TEM, JEOL JEM F200, Japan). Energy-dispersive X-ray spectrometry (EDX) was used to analyze the elemental distribution of the catalyst. The magnetic properties of the catalysts were measured with a vibrating sample magnetometer (VSM 7404, Lake Shore Company, USA). The degree of carbon order before and after P doping was analyzed by using a laser confocal Raman spectrometer (Horiba LabRAM HR Evolution, Japan) with an excitation wavelength of 532 nm. The thermal stabilities of the catalysts were analyzed using a simultaneous thermal analyzer (HITACHI STA200, Japan), heating from room temperature to 800 °C at 5 °C/min under a N_2 atmosphere. The crystalline structures of the catalysts were analyzed through X-ray diffraction (XRD) with a Rigaku Ultima IV diffractometer (Japan) using Cu Kα radiation of 40 kV. Fourier transform infrared spectra (FT-IR) to characterize functional groups of the catalysts were acquired through a Thermo Scientific Nicolet Is50 spectrometer (Thermo Fisher, USA). X-ray photoelectron spectroscopy (XPS) was used to analyze the surface molecular structure of the catalysts, which was performed on an Axis Ultra DLD spectrometer (Kratos, UK) using Al−Kα X-ray radiation. NH_3 temperature-programmed desorption (NH_3-TPD) was conducted on Auto Chem II 2920 equipment (Micromeritics, USA) to investigate the acid strength of the catalysts. In situ FTIR spectra of pyridine (Py-FTIR) were acquired on a Bruker Tensor 27 instrument (Germany) to analyze acid types (Brønsted/Lewis acid) of the catalysts. An inductively coupled plasma optical emission spectrometer (ICP-OES, Agilent 5110, USA) was used to measure the P contents of catalysts.

Liquid Product Analysis. The quantitative analysis of liquid products was carried out using high-performance liquid chromatography (HPLC, SHIMADZU LC-20, Japan). This instrument was equipped with a Bio-Rad Aminex HPX-87H column, an SPD-20 UV-vis detector, and an RID-10A refractive index detector. The column oven and detector were maintained at temperatures of 50 and 35 °C, respectively. The mobile phase used was 0.005 M H_2SO_4, with a flow rate of 0.6 mL/min. The liquid product yield, xylose yield (calculated based on the weight of hemicellulose), and xylose selectivity were calculated using the relevant eqs 1 to 3.

$$\text{Liquid product yield (\%)} = \frac{\text{Liquid product weight (g)}}{\text{Starting material weight (g)}} \times 100\% \quad (1)$$

$$\text{Xylose yield (\%)} = \frac{\text{Xylose weight (g)}}{\text{Hemicellulose weight in Starting material (g)}} \times 100\% \quad (2)$$

$$\text{Xylose selectivity (\%)} = \frac{\text{Xylose weight (g)}}{\text{Total weight of small molecular products (g)}} \times 100\% \quad (3)$$

DFT Calculation. All density functional theory (DFT) calculations were performed using the DMol3 package in Materials Studio 2024 at the default 0 K limit. Exchange-correlation effects were treated with the generalized gradient approximation (GGA)[21] via the Perdew−Burke−Ernzerhof (PBE) functional. Core electrons of Fe atoms were represented by effective core potentials (ECPs),[22] while all-electron calculations were employed for C, Si, H, P, and O atoms. The double numerical plus polarization (DNP) basis set was adopted with strict convergence criteria: energy convergence $<2.0 \times 10^{-5}$ hartree and maximum atomic displacement $<5.0 \times 10^{-3}$ Å. The DFT calculations considered dispersion corrections (DFT-Grimme) and solvation effects (H_2O), with H_2O as the reactant molecule, to construct an explicit solvent model. The total energy represents the total amount of the calculated structure in the calculations.

RESULTS AND DISCUSSIONS

Catalytic Performance of Various P-Doped Magnetic Solid Catalysts. Four types of core−shell magnetic solid catalysts, including MSi (silica-coated Fe_3O_4), MC (silica−carbon-coated Fe_3O_4), MSiP (P-doped MSi), and MC_xP_y (P-doped MC), were synthesized through carbonization at 600 °C for 2 h, with their respective images shown in Figure 1A. The hydrothermal catalytic transformation of xylan, simulating hemicellulose in biomass, to produce xylose at 100 °C for 2 h was initially conducted by using these core−shell catalysts, with the results detailed in Figure 1B. In the absence of a catalyst, the xylose yield was only 2.3%. The addition of MSi resulted in a similar xylose yield, indicating the limited catalytic effect of the silica layer on xylose production. Such a negligible catalytic effect confirms that the silica layer is catalytically inert for xylan hydrolysis under these conditions. Its surface silanol (Si−OH) groups possess insufficient Brønsted acidity to cleave the β-1,4-glycosidic bonds in xylan effectively. Conversely, using MC slightly raised the xylose yield to 9.6%. The creation of oxygen-containing acidic functional groups (−OH and −COOH) on the carbon layer through high-temperature carbonization facilitated xylan hydrolysis into xylose, as these sites can donate protons to facilitate hydrolysis. However, their limited density and acid strength constrain the overall conversion.[16,23]

A dramatic catalytic enhancement was achieved through P doping. The xylose yields surged to 58.8% for MSiP and 70.5% for $MC_{600}P_{1.0}$, demonstrating that P incorporation was the key to unlocking the high activity. The treatment with H_3PO_4 and subsequent thermal activation generated thermally stable P-containing acid species (e.g., C−O−P or polyphosphoric acids). These species are significantly more acidic than the native functional groups on carbon or silica, thus vigorously accelerating the hydrolysis reaction. Moreover, $MC_{600}P_{1.0}$ achieved an 11.7% greater yield compared to MSiP. This highlights a crucial synergistic effect between the carbon layer and the P dopant. The carbon layer provides a superior scaffold for anchoring and dispersing the P species, while H_3PO_4 simultaneously functions as a chemical activating agent, altering the structure of the carbon support. This improved texture enhances accessibility to the acid sites, leading to superior catalytic performance.

Finally, the structural integrity of the catalysts was assessed. An analogous catalyst with a carbon shell directly coating the Fe_3O_4 core (without silica) suffered from severe degradation during P-doping, consequently losing its magnetism. This seems to confirm that, despite the silica layer being catalytically passive, it plays an indispensable role as a protective shield, as it prevents Fe_3O_4 from being attacked by H_3PO_4 during the synthesis, thus preserving the catalytic structure and the essential superparamagnetic properties for magnetic separation.

After establishing the superiority of P-doped MC, a detailed study was conducted to optimize its synthesis. Different formulations, designated as MC_xP_y, were prepared by system-

https://doi.org/10.1021/acssuschemeng.5c11136
ACS Sustainable Chem. Eng. XXXX, XXX, XXX−XXX

atically varying the H_3PO_4 concentration (y), activation temperature (x), and activation time to maximize the xylose yield. The amount of H_3PO_4 used in the doping process demonstrated a distinct saturation effect, as shown in Figure 1C. The xylose yield progressively increased as the acid ratio was raised from 0.3 mL/g (50.6% yield) to a peak of 86.9% at 1.2 mL/g. This initial increase is due to the greater availability of P to react with the carbon support, thereby increasing the density of catalytically active P-containing species.[24] Beyond 1.2 mL/g, the yield plateaued, indicating that the carbon surface had become saturated with active sites. This point represents the optimal loading, as adding more acid provides no further catalytic benefit, probably because all reactive sites on the support have already been functionalized. The activation temperature exhibited a classic volcano-shaped trend, with optimal performance achieved at 600 °C (Figure 1D). At a low temperature of 300 °C, the catalyst showed a surprisingly high yield (77.4%), likely due to residual, unreacted H_3PO_4 on the surface acting as a liquid acid catalyst. The subsequent drop in activity at 400 °C (73.6%) suggests a transition state where the residual acid has been driven off, but the temperature is still too low for the efficient formation of stable, covalently bonded P-containing acid sites. The peak activity at 600 °C marks the ideal temperature for chemical activation. Here, H_3PO_4 dehydrates to form polyphosphoric acids, which then react with the carbon to create a high density of strongly acidic, thermally stable P-containing species while simultaneously developing the catalyst's porous structure.[25] Above 600 °C, the yield declined due to the thermal degradation of these active P-containing species, reducing the overall acidity and performance of the catalyst. The activation time at the optimal temperature of 600 °C had a meager influence on the catalytic activity (Figure 1E). The highest xylose yield was achieved with an activation time of 1 h. This indicates that the key chemical reactions for forming the active sites are relatively quick at such a temperature. From a practical viewpoint, this is a highly favorable outcome, as a shorter duration enhances process efficiency and lowers energy consumption. Based on this comprehensive optimization, the catalyst ($MC_{600}P_{1.2}$) prepared at 600 °C with an acid ratio of 1.2 mL/g for 1 h was identified as the most effective formulation.

With the optimal catalyst, $MC_{600}P_{1.2}$, the reaction parameters were systematically optimized to maximize the xylose yield. This involved evaluating the influence of the reaction temperature, time, and catalyst loading (Figure 1F−H). The reaction temperature displayed a distinct optimal point. As shown in Figure 1F, increasing the temperature from 60 to 100 °C boosted the xylose yield from 15.0% to a peak of 86.9%. This initial rise is expected, as higher temperatures accelerate the kinetic rate of the desired xylan hydrolysis reaction. However, further increasing the temperature to 140 °C caused a sharp drop in yield to 54.6%. This is a classic outcome of the competing relationship between product formation and degradation or repolymerization. A similar trend was observed for the reaction time (Figure 1G). The xylose yield increased steadily until it reached its maximum at 2 h. Extending the reaction time to 4 h resulted in a lower yield. In the initial phase, xylan hydrolysis is the dominant reaction. However, once a significant concentration of xylose has accumulated, it becomes the primary reactant for the subsequent degradation reaction, allowing xylose to be converted into undesirable byproducts. The amount of catalyst used also showed an optimal value, peaking at 0.10 g (Figure 1H). Increasing the catalyst loading initially provides more active sites, accelerating the conversion of xylan to xylose. However, using an excessive amount of catalyst (>0.10 g) proves to be counterproductive. A very high concentration of acid sites makes the hydrolysis reaction extremely fast, but it also dramatically accelerates the degradation of the newly formed xylose. Based on this systematic optimization, the maximum xylose yield of 86.9% was achieved under the following optimal conditions: a reaction temperature of 100 °C, a reaction time of 2 h, and a catalyst amount of 0.10 g.

In the process of xylan acid hydrolysis, xylose was the dominant C5 sugar, and almost no arabinose was detected, which may be attributed to the specific source and structure of the commercial xylan used (Figure S1). Xylose isomers, such as xylulose, are typically considered intermediates in the dehydration of xylose to furfural. Their formation generally requires high temperatures (>160 °C) and basic conditions.[26,27] Under the current acidic environment and low temperature (100 °C), no furfural was detected, and only trace amounts of formic acid (<0.5%) were observed as byproducts. Furthermore, kinetic experiment results showed that the rate constant k_1 (0.0377 min^{-1}) is much larger than that of k_2 (0.0005 min^{-1}), indicating that xylan hydrolysis to xylose is the dominant step, which is consistent with the high xylose yield and the very low level of byproducts observed in this system (Figure S3 and Table S2). Therefore, the isomerization of xylose to xylulose and its further conversion to furfural was strongly suppressed, indicating the high selectivity of xylose formation in this catalytic system.

Catalytic Saccharification of Hemicellulose in Biomass. Having proven its efficacy on pure xylan, the optimized $MC_{600}P_{1.2}$ catalyst was used for the hydrothermal catalytic conversion of various hemicellulose-rich biomasses, such as corncob, corn stover, poplar, and bamboo. The optimization of the reaction temperature for 2 h using corn stover as the representative feedstock was first studied, and the results confirmed that 160 °C with $MC_{600}P_{1.2}$ was the optimal condition for xylose production (Figure S4). This identical reaction condition was then applied to other biomass types to evaluate the general applicability of the catalyst. As shown in Figure 2A and Table S3, the reaction products obtained comprised small molecular products such as aldehydes (e.g., furfural and 5-hydroxymethylfurfural), carboxylic acids (e.g., formic acid, acetic acid, and lactic acid), and sugars (e.g., xylose, glucose, and arabinose). The total yields of these small-molecule products were predictably low, ranging from just 4.7% for poplar to 12.6% for corncob. This highlights the inherent recalcitrance of lignocellulosic biomass. The introduction of the $MC_{600}P_{1.2}$ catalyst dramatically enhanced the conversion. The total yield of small-molecular products increased across all feedstocks, with corncob achieving the highest total yield of 42.6%. This powerful performance confirms that the catalyst is highly effective at deconstructing the complex hemicellulose matrix within the native plant structure. Furthermore, the catalyst displayed remarkable efficiency and selectivity for producing xylose from the hemicellulose fraction of each biomass (Figure 2B,C). Based on the weight of hemicellulose in biomass, the xylose yield reached 85.5%, 60.3%, 91.0%, and 69.2% from corncob, corn stover, poplar, and bamboo, respectively. The optimal conditions for xylose production varied across different biomass feedstocks. Such variations are expected and can be

https://doi.org/10.1021/acssuschemeng.5c11136
ACS Sustainable Chem. Eng. XXXX, XXX, XXX−XXX

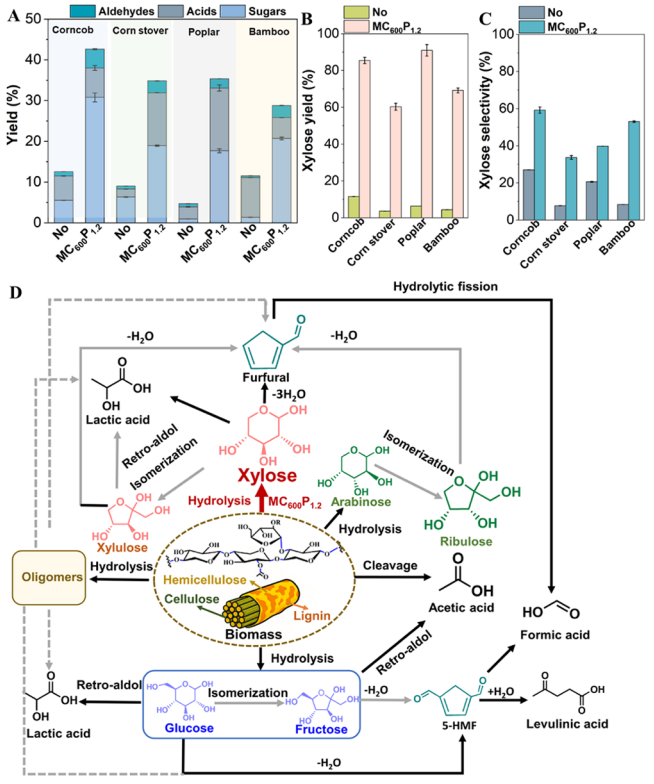

Figure 2. Small-molecular product yield (A), xylose yield (B), and xylose selectivity (C) from various biomass in the absence and presence of $MC_{600}P_{1.2}$; (D) the proposed reaction network of major products from hemicellulose in biomass.

attributed to the inherent differences in the structural complexity and composition (e.g., lignin content and type, hemicellulose accessibility, biomass extractives) of each biomass type.[28] The exceptional performance of the $MC_{600}P_{1.2}$ catalyst on diverse, unprocessed biomass feedstocks demonstrates its strong potential for practical application in sustainable biorefineries, paving the way for more efficient valorization of hemicellulose into valuable platform chemicals.

Actually, hemicellulose depolymerization proceeds via a highly complex reaction network, as shown in Figure 2D. Briefly, hemicellulose was first hydrolyzed into soluble oligomers, which were further cleaved into monomeric sugars, predominantly xylose, with minor amounts of arabinose (Figure S2). C5 sugars may undergo acid-catalyzed dehydration to form furfural, which was further converted to formic acid through hydrolytic fission of the aldehyde group. Acetic acid mainly originated from the cleavage of the acetyl groups in hemicellulose. Because hemicellulose contains both C5 and C6 units, a small amount of glucose (3.4−6.3%) was also detected. Glucose can be dehydrated to 5-HMF, which is subsequently transformed into levulinic acid and formic acid. Lactic acid formation may arise from both C5 and C6 sugars via retro-aldol reactions. In addition, some of these small molecules (e.g., lactic acid and furfural) may also arise directly from the transformation of sugar oligomers. During the sugar conversion process, isomers, such as xylulose, are likely formed but rapidly converted into downstream products, which explains why no sugar isomers were detected. Although $MC_{600}P_{1.2}$ exhibited excellent activity and selectivity for xylose production across various biomass feedstocks, the formation of these byproducts from hemicellulose was difficult to completely avoid. Future work will focus on further optimizing the reaction conditions and tailoring the catalyst properties to enhance xylose selectivity. Additionally, in situ sugar protection through reversible acetal formation with trapping agents (e.g., formaldehyde) can effectively prevent subsequent degradation pathways.[29]

These results represent a significant advancement in the field. As illustrated in Table S4, this study adopts pure water as the solvent with a novel magnetically P-doped solid acid catalyst, in contrast to other methodologies that rely on corrosive acids or costly enzymes. Solid acid catalysts capable of efficiently producing xylose from raw biomass are still rare. For instance, the xylose yield of 85.5% achieved from corncob in this study outperforms the 74.9% yield reported by Qi et al. using a different MMCSA solid catalyst under similar conditions.[16] Unlike conventional solid acid catalysts, they relied on sulfonation, which suffered from high corrosivity due to concentrated sulfuric acid and unavoidable leaching. This work addressed these limitations by developing a robust, magnetically separable, P-doped core−shell catalyst that achieved efficient hemicellulose saccharification under mild conditions, advancing cleaner and more efficient biorefining.

Catalyst Reusability. The stability and reusability of a heterogeneous catalyst are paramount for its practical and industrial viability. Therefore, the performance of the optimal $MC_{600}P_{1.2}$ catalyst was evaluated over multiple reaction cycles (Figure 3A and B). After each round of xylan hydrolysis, the catalyst was separated using an external magnet and directly dried for subsequent use. During the hydrolysis of pure xylan at 100 °C for 2 h, a notable decrease in xylose yield was observed, from 86.9% with the fresh catalyst to 62.5% after the first cycle, whereupon the activity remained stable through the third run. A similar trend was also observed in the poplar hydrolysis system. This deactivation behavior suggests a dual mechanism. The marked initial drop correlates well with a decrease in the P content of the catalyst, which fell from 24.1% (fresh) to 19.4% after three runs in the poplar hydrolysis system (Figure 3C), according to ICP analyses. This suggests that a minor fraction of loosely bound or less stable P-containing species likely leaches into the aqueous phase during the initial reaction.

After this initial leaching, the subsequent stable activity (or the gradual decline seen with poplar hydrolysis) can be accounted for by the progressive deactivation caused by fouling due to the deposition of humins, i.e., polymeric byproducts of sugar degradation, onto the surface of the catalysts.[30] Two key findings corroborate this fouling hypothesis. On the one hand, simple water washing was ineffective for regeneration; the water-washed catalyst ($MC_{600}P_{1.2}$-W_3) yielded 62.3% xylose, a value statistically identical to the unwashed used catalyst, which is consistent with the hydrophobic and insoluble nature of humin polymers. These developments suggest that the water washing step used to synthesize the $MC_{600}P_{1.2}$ catalyst did not enhance its catalytic activity.

On the other side, the thermal regeneration conducted via recarbonization at 600 °C for 2 h proved to be remarkably effective. In particular, the regenerated catalyst ($MC_{600}P_{1.2}$-R_3) restored the xylose yield from xylan to 81.6%. When applied after each cycle of poplar hydrolysis, this strategy resulted in consistently high xylose yields (93.3%, 93.6%, and 92.5%) over three consecutive cycles (Figure 3B). This indicated that recarbonization significantly boosted the catalytic activity of used $MC_{600}P_{1.2}$, representing a promising strategy to maintain high catalytic activity.

https://doi.org/10.1021/acssuschemeng.5c11136
ACS Sustainable Chem. Eng. XXXX, XXX, XXX−XXX

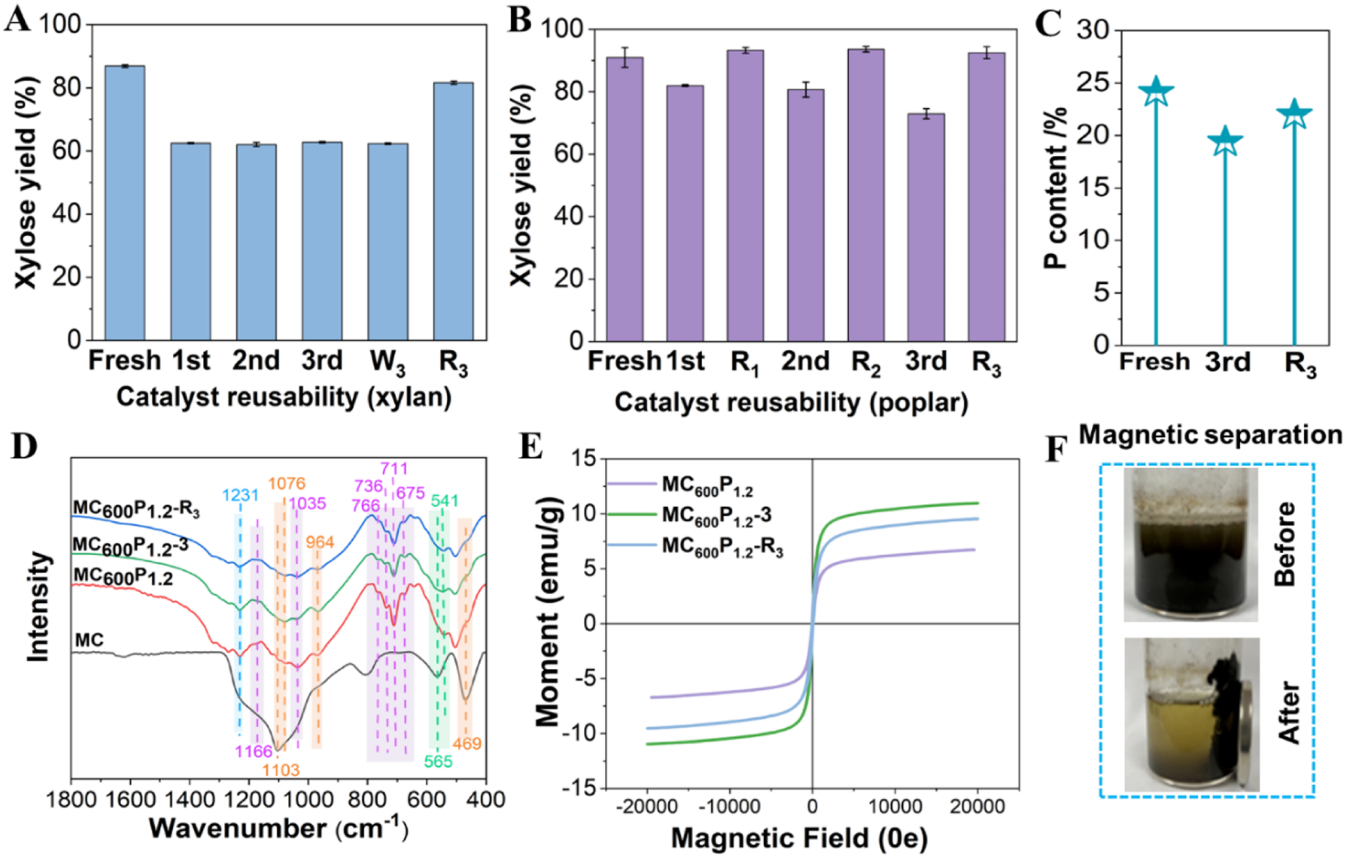

Figure 3. Reusability performance of $MC_{600}P_{1.2}$ in the optimal hydrothermal catalytic depolymerization of xylan at 100 °C for 2 h (A) and poplar at 160 °C for 2 h (B); ICP-OES results of P contents in various catalysts for the poplar hydrolysis system (C); magnetic hysteresis curves (D) and FT-IR spectra (E) of fresh and used catalysts; the picture of catalyst separation from hydrolyzate with an external magnet (F).

The complete set of ICP-OES data provides a cohesive explanation for these observations. The thermal treatment effectively pyrolyzes and removes the deposited organic humins but cannot restore the P lost to leaching, as the P content of the regenerated catalyst (22.0%) did not fully return to its original value (24.1%), as shown in Figure 3C. Taken together, these results demonstrate that catalyst deactivation is governed by a minor, irreversible loss of P species, followed by a dominant, reversible fouling by humins. The preparation of P-doped catalysts typically employs the impregnation-carbonization method, using P precursors (e.g., $(NH_4)_2HPO_4$, H_3PO_4) and carbon sources.[17,18,31,32] In contrast, the P-doped catalyst developed in this work additionally incorporated an Fe_3O_4 magnetic core and an acid-resistant silica interlayer, with a P-doped carbon shell to form a unique core−shell architecture. Compared with the fresh catalyst, the FT-IR peaks assigned to P-containing groups at 766−1166 cm^{-1} for both $MC_{600}P_{1.2}$-3 and $MC_{600}P_{1.2}$-R_3 remained essentially unchanged, demonstrating their significant stability as formed in $MC_{600}P_{1.2}$[33,34] (Figure 3D). $MC_{600}P_{1.2}$-3 and $MC_{600}P_{1.2}$-R_3 obtained from the poplar hydrolysis system, both exhibited similar XRD patterns to that of $MC_{600}P_{1.2}$, further confirming the stable properties of the catalyst (Figure S5). $MC_{600}P_{1.2}$ exhibited a saturation magnetization intensity of 6.7 emu/g (Figure 3E), which was sufficient for its separation and recovery from the biomass reaction system using an external magnet (Figure 3F).[16] Furthermore, the saturation magnetization intensities of $MC_{600}P_{1.2}$-3 and $MC_{600}P_{1.2}$-R_3 were 11.0 and 9.5 emu/g, respectively, which were even slightly higher than that of fresh $MC_{600}P_{1.2}$. This indicated that the catalyst retained good magnetism after three runs and that its magnetism was not significantly affected by the regeneration process. The exceptional core−shell structural stability of the covalently bound P-containing active species, combined with a straightforward and highly effective regeneration protocol, underscores the robust potential of the $MC_{600}P_{1.2}$ catalyst for application in sustainable biorefinery processes.

Physical and Chemical Structures of P-Doped Magnetic Solid Catalysts. To explore the effects of P doping on the physical and chemical structures of the catalysts, we first employed SEM to analyze the morphologies of MC and $MC_{600}P_{1.2}$. As shown in Figure 4A, many uniform and regular spherical particles, identified as Fe_3O_4, were observed on the smooth surface of MC. After P doping, a rough surface without Fe_3O_4 spheres was observed (Figure 4B), possibly due to the thermal expansion of a silica−carbon layer via high-temperature carbonization that encased the Fe_3O_4 particles. TEM images reveal that MC displayed particle agglomeration due to magnetic interactions (Figure 4C).[35] This silica−carbon structure not only provided an ideal scaffold to better anchor P to enhance the stability of the catalyst but also avoided particle agglomeration and facilitated more uniform dispersion of the catalyst particles (Figure 4D). These features, in turn, potentially enhanced the catalyst's interactions with reactants and boosted its catalytic activity. For the MC, the measured lattice fringes corresponded to the (400) plane of Fe_3O_4 (Figure 4E). By comparison, $MC_{600}P_{1.2}$ showed lattice fringes matching the (222), (400), (422), and (511) planes of Fe_3O_4

https://doi.org/10.1021/acssuschemeng.5c11136
ACS Sustainable Chem. Eng. XXXX, XXX, XXX−XXX

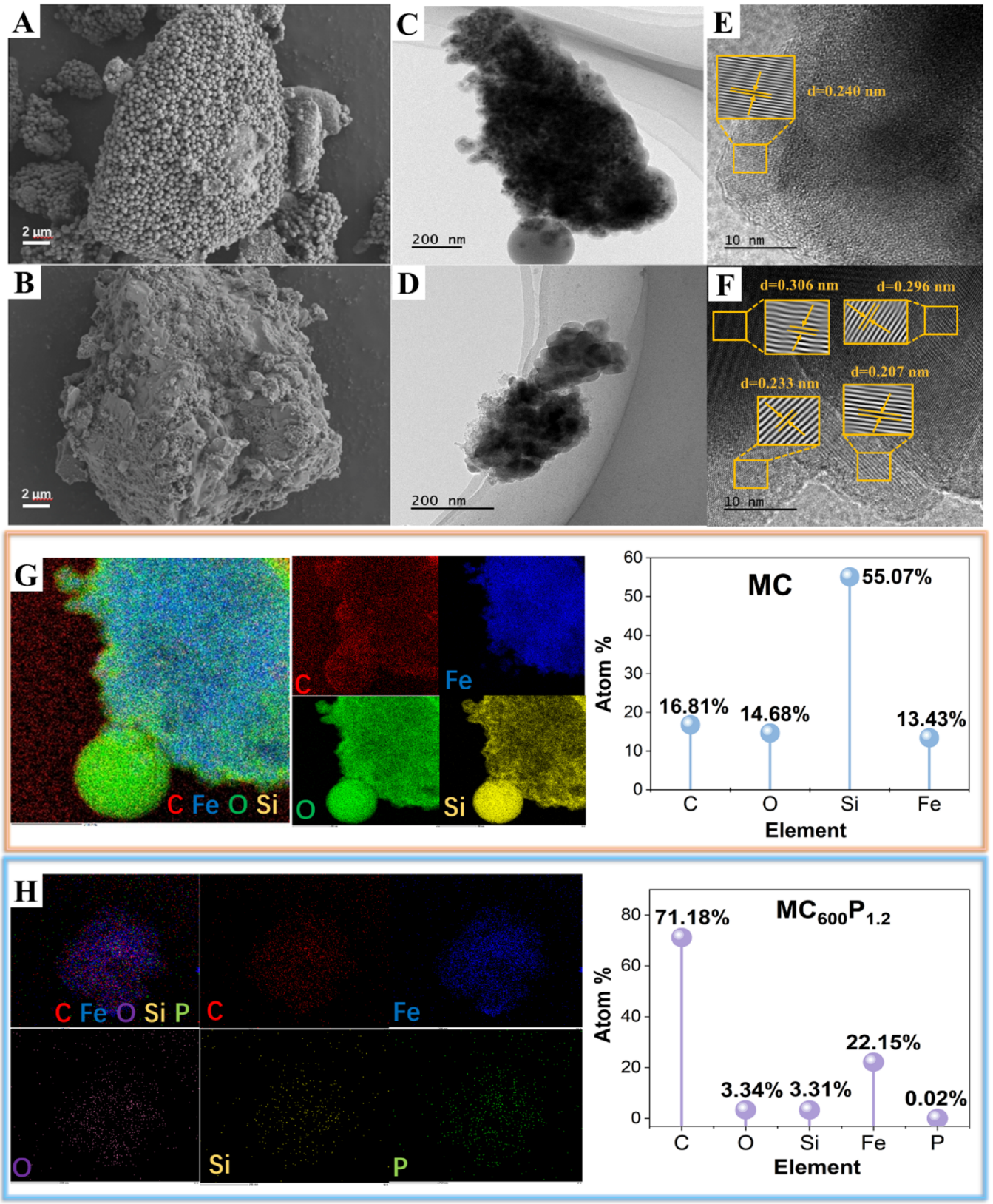

Figure 4. SEM images of MC (A) and $MC_{600}P_{1.2}$ (B); TEM and HRTEM images of MC (C and E) and $MC_{600}P_{1.2}$ (D and F); energy-dispersive X-ray mapping images and corresponding element contents of MC (G) and $MC_{600}P_{1.2}$ (H).

(Figure 4F). These observations aligned with the formation of a protective layer on Fe_3O_4, which hindered agglomeration, thereby exposing more Fe_3O_4 planes. Figure 4G and H shows the element distribution of MC and $MC_{600}P_{1.2}$, as detected by EDX mapping, confirming that the C, O, Fe, Si, and P elements were uniformly distributed in the catalysts, and P was successfully doped in $MC_{600}P_{1.2}$.

https://doi.org/10.1021/acssuschemeng.5c11136
ACS Sustainable Chem. Eng. XXXX, XXX, XXX−XXX

Raman spectra of MC and $MC_{600}P_{1.2}$ shows two peaks representing disordered carbon (D peak) and sp²-hybridized graphite carbon (G peak) at about 1361 and 1586 cm^{-1}, respectively.[19] Compared to MC, slight shifts of the D peak from 1361 to 1356 cm^{-1} and the G peak from 1586 to 1590 cm^{-1} were observed for $MC_{600}P_{1.2}$ (Table S5). The I_D/I_G of $MC_{600}P_{1.2}$ (0.879) was slightly greater than that of MC (0.782), as shown in Figure 5A. Patel et al. reported that the

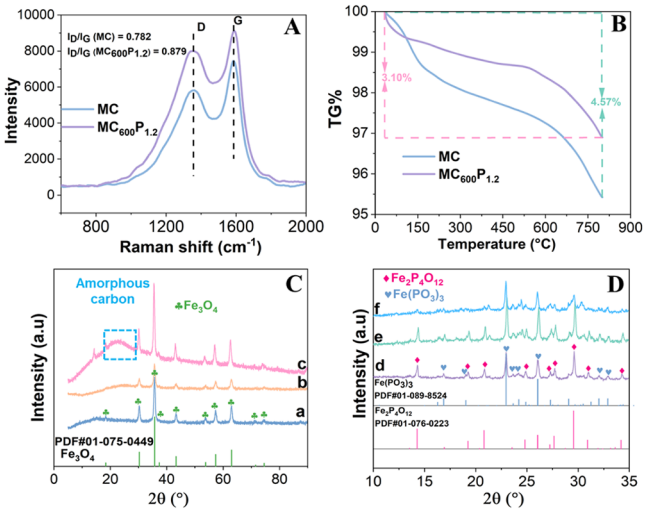

Figure 5. Characterization of P-doped magnetic solid catalysts: (A) Raman spectra; (B) TG curves; (C and D) XRD patterns (a, Fe_3O_4; b, Fe_3O_4@SiO_2; c, MC; d, $MC_{600}P_{1.2}$; e, $MC_{600}P_{1.2}$-3; f, $MC_{600}P_{1.2}$-R_3).

incorporation of P disrupted the hexagonal symmetry of the graphene plane, increasing the intensity of the D band in Raman spectra.[33] This implied that P doping altered the carbon layer structure and marginally increased the defects in the graphitic structure, which could offer potential active sites for adsorbing biomass materials.[36,37] Thermogravimetric analysis showed that under a N_2 atmosphere, $MC_{600}P_{1.2}$ exhibited only a mass loss of 3.10%, while MC displayed a 4.57% reduction at 800 °C (Figure 5B). This demonstrated that both samples had high thermal stabilities, with P doping further enhancing the catalyst's resistance to thermal degradation.

Figure 5C,D shows the XRD patterns of various magnetic solid catalysts. The diffraction peaks at 2θ of 18.5°, 30.4°, 35.8°, 37.4°, 43.5°, 53.9°, 57.5°, 63.2°, 71.7°, and 74.8° were assigned to the (1 1 1), (2 2 0), (3 1 1), (2 2 2), (4 0 0), (4 2 2), (5 1 1), (4 4 0), (6 2 0), and (5 3 3) lattice planes of Fe_3O_4 (PDF#01-075-0449), respectively. There were no obvious changes in the diffraction peaks assigned to Fe_3O_4 for Fe_3O_4@SiO_2 and MC, while MC had a broad diffraction peak at 2θ = 22.4°, corresponding to amorphous carbon, which confirmed the successful introduction of the carbon layer onto the catalyst. For $MC_{600}P_{1.2}$, the presence of these Fe_3O_4 diffraction peaks indicated that P doping did not affect the magnetic structure of the catalyst (Figure S5). Additionally, diffraction peaks observed at 2θ = 12°−35°, associated with $Fe_2P_4O_{12}$ (PDF#01-076-0223) and $Fe(PO_3)_3$ (PDF#01-089-8524), were formed on $MC_{600}P_{1.2}$. These diffraction peaks were also observed for $MC_{600}P_{1.2}$-3 and $MC_{600}P_{1.2}$-R_3. By employing $MC_{600}P_{1.2}$Fe (P and Fe-doped MC, see Supporting Information), the xylose yield from poplar reached 69.1% after being treated at 160 °C for 2 h, a result significantly inferior to the 91.0% that was achieved with $MC_{600}P_{1.2}$. This indicated that the elevated catalytic activity of $MC_{600}P_{1.2}$ was not associated with the formation of phosphoferric compounds.

In the FT-IR spectra of MC presented in Figure 3D, the peak at 565 cm^{-1} was assigned to the stretching vibration of Fe−O, indicating the presence of Fe_3O_4 core, which was consistent with the XRD analysis.[15] The peaks at 469, 964, 1076, and 1103 cm^{-1} represented the stretching vibration of Si−O−Si, indicating the successful incorporation of a silica layer.[38−40] $MC_{600}P_{1.2}$ showed a reduction and shift in these characteristic peaks, likely due to structural changes in the carbon coating after P doping, as also evidenced by the morphological changes seen in SEM. Notable peaks of P-containing groups appeared at 1166 (P═O), 1035 (C−O−P), 663−750 (C−P), and 766 cm^{-1} (P−OH),[33,34] suggesting the formation of these P-containing species through the interaction of the carbon shell and H_3PO_4.

Additionally, the molecular structures of P contained in $MC_{600}P_{1.2}$ were studied via deconvolution of P_{2p} peaks, as displayed in Figure 6A. Three peaks assigned to phosphorus oxides (PO_x) at 132.1 eV (C_3−P═O), 133.1 eV (C−P−O), and 134.0 eV (C−O−P) appeared, respectively, corresponding to percentages of 59.4%, 27.8%, and 12.8% (Table S6). The C_{1s} XPS spectra showed five peaks at 282.8, 284.5, 286.2, 287.8, and 288.9 eV, corresponding to Si−C, C═C/C−C (aromatic rings), C−O (phenolic, alcohol, and ether), C═O (carbonyl), and C═O−O (carboxyl and ester) groups (Figure 6B).[41,42] Compared with MC, P doping facilitated the formation of Si−C, as its concentration significantly increased from 3.4% to 36.3% (Table S7). Conversely, the relative contents of C═C/C−C, C−O, C═O, and C═O−O in $MC_{600}P_{1.2}$ decreased by 11.7%, 15.3%, 3.3%, and 2.6%, respectively. This indicates strong interactions between P and carbon-containing groups. The O_{1s} XPS spectra were fitted with five peaks at 529.8 (Fe−O), 530.8 (C═O, carbonyl), 532.1 (C−O, hydroxyl or ether), 532.8 (SiO_2), 533.5 (C═O−O, carboxylic acid, anhydride, or lactone),[41,43] as shown in Figure 6C. Consistent with the C_{1s} XPS results, the relative concentration of SiO_2 decreased from 28.5% in MC to 1.7% in $MC_{600}P_{1.2}$, likely due to the formation of Si−C after P doping. Compared to MC, the relative concentrations of C−O and C═O−O significantly decreased in $MC_{600}P_{1.2}$, along with a remarkable increase in the relative concentrations of Fe−O and C═O from 2.3% and 11.5% to 54.7% and 36.6%, respectively (Table S8).

The binding energy at 530.8 ± 0.3 eV was assigned to PO_x, overlapping with Fe−O and C═O, which led to an increase in their relative concentrations.[31] The linkage of P species to oxygen functional groups on nanocarbon material surfaces predominantly appears as PO_x, functioning as both electronic modulators and active sites.[31,44] Consequently, the PO_x (C−P−O, C_3−P═O, C−O−P) formed through interactions between P and carbon/oxygen-containing groups served as catalytically active sites in $MC_{600}P_{1.2}$, facilitating the saccharification of hemicellulose in biomass.

Catalytic Mechanism of Hemicellulose Saccharification over P-Doped Solid Catalyst. The depolymerization of hemicellulose in biomass to xylose through the cleavage of glycosidic bonds generally requires an acidic environment. NH_3-TPD and Py-FTIR analyses were conducted to assess the acid strength and the acid types of catalysts. According to the NH_3 desorption temperature, acid sites were classified as weak

https://doi.org/10.1021/acssuschemeng.5c11136
ACS Sustainable Chem. Eng. XXXX, XXX, XXX−XXX

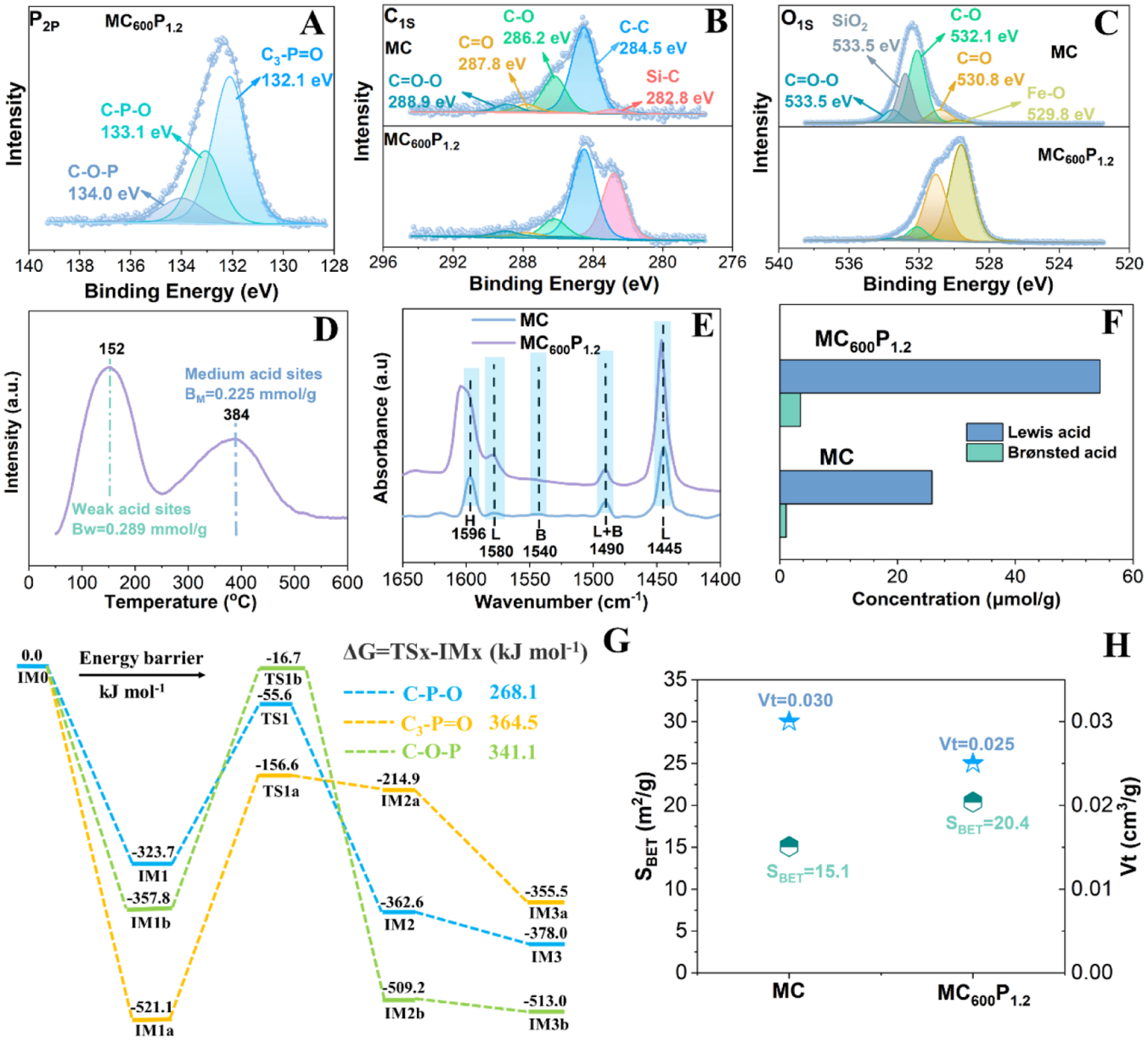

Figure 6. P_{2p} (A), C_{1s} (B), and O_{1s} (C) XPS spectra of P-doped magnetic solid catalysts; NH_3-TPD spectra of $MC_{600}P_{1.2}$ (D); in situ FTIR spectra of pyridine of MC and $MC_{600}P_{1.2}$ at 150 °C (E) and the corresponding acid distributions (F); energy barrier of xylobiose to xylose with PO_x (G); specific surface area (S_{BET}) and pore volume (Vt) of MC and $MC_{600}P_{1.2}$ (H).

(100−250 °C), medium (250−500 °C), and strong acid sites (above 500 °C).[45] The $MC_{600}P_{1.2}$ showed two peaks centered at 152 and 384 °C, ascribed to the weak and medium acid sites, respectively (Figure 6D). As shown in Figure 6E, Py-FTIR spectra of MC showed characteristic peaks at 1445 cm^{-1} (strong Lewis acid sites), 1580 cm^{-1} (weak Lewis acid sites), and 1490 cm^{-1} (Lewis and Brønsted acid sites).[46] In $MC_{600}P_{1.2}$, these characteristic peaks increased markedly, with the peak at 1445 cm^{-1} slightly shifted to 1447 cm^{-1}. Compared to that in MC, the concentration of Lewis acid sites in $MC_{600}P_{1.2}$ significantly increased from 25.9 to 54.4 μmol/g, along with a slight increase in the concentration of Brønsted acid sites from 1.08 to 3.52 μmol/g (Figure 6F). This suggested that P doping introduced PO_x species as new Lewis acid sites. Moreover, the peak at 1596 cm^{-1} (hydrogen-bonded pyridine) was notably higher in $MC_{600}P_{1.2}$ than in MC. This implied that $MC_{600}P_{1.2}$ might offer more hydrogen-bonding sites, potentially enhancing its adsorption on biomass and improving the catalytic activity with the newly formed PO_x.

The catalytic mechanisms of PO_x as Lewis acids formed on $MC_{600}P_{1.2}$ for biomass hemicellulose saccharification were further investigated. DFT calculations helped construct a reaction energy diagram using xylobiose as a model compound for hemicellulose, demonstrating the pathways for hemicellulose saccharification with potential PO_x (C−P−O, C_3−P═O, C−O−P) catalytic species on $MC_{600}P_{1.2}$, as shown in Figure 6G and Figure 7 A. It was observed that both H_2O and xylobiose were stably adsorbed on the C−P−O, C_3−P═O, and C−O−P of $MC_{600}P_{1.2}$, leading to the formation of intermediates IM1, IM1a, and IM1b, with adsorption energies of −323.7, −521.1, and −357.8 kJ mol^{-1}, respectively, suggesting their thermodynamic favorability. As shown in Figure 6H, $MC_{600}P_{1.2}$ exhibited a limited specific surface area (S_{BET} = 20.4 m^2/g) and pore volume (Vt = 0.025 cm^3/g),

https://doi.org/10.1021/acssuschemeng.5c11136
ACS Sustainable Chem. Eng. XXXX, XXX, XXX−XXX

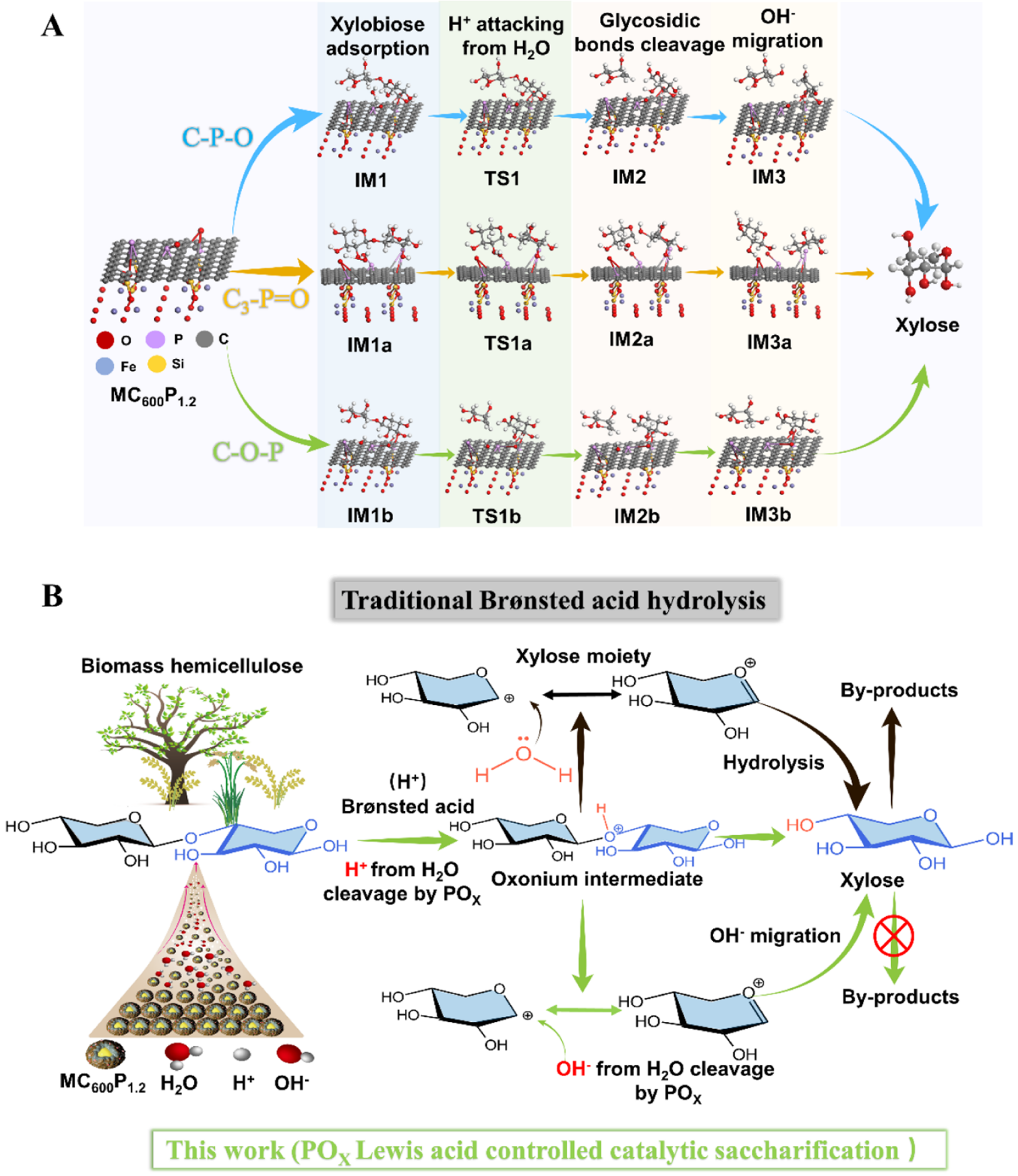

Figure 7. (A) The calculated geometries for xylobiose to xylose with possible PO_x species (C−P−O, C_3−P═O, C−O−P) on $MC_{600}P_{1.2}$; (B) the pathway of hemicellulose saccharification by traditional Brønsted acid or $MC_{600}P_{1.2}$.

which were comparable to those of MC (S_{BET} = 15.1 m^2/g and Vt = 0.030 m^2/g). H_3PO_4 is indeed a widely used chemical activator for producing highly porous carbons from lignocellulose biomass, while pore development is extremely sensitive to the H_3PO_4 dosage.[47] When the H_3PO_4 loading exceeded a certain threshold, its dehydration products, such as phosphate and polyphosphate species, could incorporate into the carbon matrix to form compounds, which partially block the porosity of carbon.[18,40,48] In this work, the P-containing species formed via H_3PO_4 activation could clog the porosity development of the catalyst, suggesting that the influence of pore adsorption was minimal. On the one hand, Raman and Py-FTIR results

https://doi.org/10.1021/acssuschemeng.5c11136
ACS Sustainable Chem. Eng. XXXX, XXX, XXX−XXX

indicated that P-doping introduced defect sites and abundant hydrogen bonding sites, which enhanced the adsorption. On the other hand, the adsorption process also involved chemisorption, as evidenced by the significant changes observed in the bond lengths of xylobiose and H_2O upon adsorption. For example, the C_1−O bond length in xylobiose changed from 1.507 Å to 1.487, 1.508, and 1.455 Å upon adsorption on C−P−O, C−O−P, and C_3−P═O, respectively (Figure S6 and Table S9). As indicated by Py-FTIR findings, $MC_{600}P_{1.2}$ predominantly consisted of Lewis acids, with a minor proportion of Brønsted acids. This indicated that the contribution of H^+ from the carbon layer of $MC_{600}P_{1.2}$ was minimal. Protons (H^+), primarily from the H−OH bond in the adsorbed H_2O, were transferred to the glycosidic oxygen atom in xylobiose, facilitating the cleavage of glycosidic bonds. This led to the formation of stable intermediates IM2 (−362.6 kJ mol^{-1}), IM2a (−214.9 kJ mol^{-1}), and IM2b (−509.2 kJ mol^{-1}), each containing a xylose molecule and a xylose moiety with energy barriers of 268.1, 364.5, and 341.1 kJ mol^{-1}, respectively. Among the three P-containing species, C−P−O emerged as the most favorable for H_2O activation in kinetics due to its lowest energy barrier. In the following step, the migration of OH^- from the cleavage of H_2O to the xylose moiety further formed a xylose with −378.0, −355.5, and −513.0 kJ mol^{-1} for IM3, IM3a, and IM3b, respectively.

Hence, it could be inferred that C−P−O, C_3−P═O, and C−O−P acted as Lewis acid sites, collectively enhancing biomass saccharification. C−P−O was particularly beneficial, as it enhanced H_2O activation to produce H^+ for glycosidic bond breaking, thereby facilitating xylose production. In traditional acid hydrolysis, the glycosidic oxygen atom was protonated by H^+ from Brønsted acid, forming an oxonium ion, followed by its decomposition and water attack to produce sugars (Figure 7B).[5] These sugars were susceptible to dehydration, resulting in the production of decomposition products. In contrast, this work developed a Lewis-acid-catalytic mechanism for hemicellulose saccharification. The PO_x (notably C−P−O) formed on $MC_{600}P_{1.2}$ acted as Lewis acid sites to facilitate H_2O activation to generate H^+, which then targeted the glycosidic oxygen atom, aiding in the cleavage of glycosidic bonds to produce xylose. Furthermore, a high yield of xylose was obtained with $MC_{600}P_{1.2}$, showcasing the controlled catalytic ability of PO_x that acted as a "protector" to prevent xylose degradation. In this work, we developed a robust, magnetically separable, P-doped core−shell catalyst that achieved efficient hemicellulose saccharification under mild conditions. The catalyst comprised a Fe_3O_4 magnetic core, an acid-resistant silica interlayer, and a phosphorus (P)-doped porous carbon shell. This unique architecture delivers a catalyst that is not only highly active but also stable and recyclable and aligns with the principles of green and sustainable catalysis. In future work, a green matrix analysis will be carried out to further evaluate the potential environmental impacts of this P-doped magnetic solid catalyst, thereby better demonstrating the sustainability and practical relevance of efficient nonenzymatic sugar production from biomass hemicellulose.[49]

CONCLUSIONS

This work has explored, for the first time, the development of a Lewis acid-controlled catalytic approach for nonenzymatic sugar production from biomass hemicellulose. Such a pioneering approach consisted of a P-doped, magnetic core−shell solid catalyst ($MC_{600}P_{1.2}$), which resulted in impressive xylose yields from xylan (86.9%, 100 °C for 2 h) and various biomasses (60.3 to 91.0%, 160 °C for 2 h) under mild hydrothermal conditions. These outstanding results were accounted for by its unique structural design, which effectively prevented particle agglomeration while maintaining good magnetism (6.7 emu/g), facilitating easy separation and delivering outstanding catalytic performance, stability, and reusability. Furthermore, this work provides substantial new insights into the catalytic roles of PO_x (C−P−O, C_3−P═O, and C−O−P) formed on $MC_{600}P_{1.2}$ in the saccharification of hemicellulose. Notably, C−P−O was the key Lewis acid to promote H_2O activation, ensuring efficient glycosidic bond cleavage. At the same time, it also acted as a protector to prevent xylose degradation. This work provides a green and sustainable approach for developing recyclable solid acid catalysts as effective alternatives to costly enzymes and homogeneous catalysts (primarily corrosive mineral acids), offering new insights for nonenzymatic sugar production from biomass hemicellulose.

ASSOCIATED CONTENT

Supporting Information

The Supporting Information is available free of charge at https://pubs.acs.org/doi/10.1021/acssuschemeng.5c11136.

Composition analysis of various biomass; catalyst preparation method; tables of literature survey; hydrolyzate analysis; kinetic experiment results; catalyst characterization; DFT calculation (PDF)

AUTHOR INFORMATION

Corresponding Author

Tianjie Ao − *Agricultural Microbial Agents Key Laboratory of Sichuan Province, Chengdu Institute of Biology, Chinese Academy of Sciences, Chengdu, Sichuan 610213, PR China;* orcid.org/0009-0009-9839-0441; Email: aotj@cib.ac.cn

Authors

Yiping Luo − *Agricultural Microbial Agents Key Laboratory of Sichuan Province, Chengdu Institute of Biology, Chinese Academy of Sciences, Chengdu, Sichuan 610213, PR China*

Bin Jiang − *Agricultural Microbial Agents Key Laboratory of Sichuan Province, Chengdu Institute of Biology, Chinese Academy of Sciences, Chengdu, Sichuan 610213, PR China*

Javier Remón − *Thermochemical Processes Group, Aragón Institute for Engineering Research (I3A), University of Zaragoza, Zaragoza 50018, Spain*

Jie Wu − *Department of Chemical and Biological Engineering, University of British Columbia, Vancouver V6T 1Z3, Canada*

Xiaoyu Zhu − *Agricultural Microbial Agents Key Laboratory of Sichuan Province, Chengdu Institute of Biology, Chinese Academy of Sciences, Chengdu, Sichuan 610213, PR China*

Fang Deng − *Agricultural Microbial Agents Key Laboratory of Sichuan Province, Chengdu Institute of Biology, Chinese Academy of Sciences, Chengdu, Sichuan 610213, PR China*

Hongquan Fu − *Precise Synthesis and Function Development Key Laboratory of Sichuan Province, Institute of Applied Chemistry, College of Chemistry and Chemical Engineering, China West Normal University, Nanchong, Sichuan 637000, PR China;* orcid.org/0000-0001-5474-7052

Dong Li − *Agricultural Microbial Agents Key Laboratory of Sichuan Province, Chengdu Institute of Biology, Chinese*

Academy of Sciences, Chengdu, Sichuan 610213, PR China; orcid.org/0000-0002-8581-8658

Complete contact information is available at: https://pubs.acs.org/10.1021/acssuschemeng.5c11136

Author Contributions

Y.L.: Formal analysis, Data processing, Writing—original draft, Writing—review and editing, Project administration; B.J.: Methodology, Investigation, Data processing; J.R.and J.W.: Data processing, Writing—review and editing; X.Z., F.D., and H.F.: Formal analysis, Data processing; T.A. and D.L.: Writing—review and editing, Supervision. All authors approved the final version of the manuscript and contributed to the scientific discussion.

Notes

The authors declare no competing financial interest.

■ ACKNOWLEDGMENTS

This work is financially supported by the National Natural Science Foundation of China (32301538), the Science and Technology Support Program of Sichuan Province (2023NSFSC0347 and 2023ZYD0280), and the Chengdu Institute of Biology, Chinese Academy of Sciences (E4S3130001 and QNTS2025-2). Javier Remón thanks MCIN/AEI/10.13039/501100011033 and the European Union ≪NextGenerationEU≫/PRTR≫ for the Ramón y Cajal Fellowship (RYC2021-033368-I) awarded, and MICIU/AEI/10.13039/501100011033 and ERDF/EU (Project PID2023-149750OA-I00) and the Aragón Government (Research Group Reference T22_23R) for providing framework support.

■ ABBREVIATION

MC microcrystalline cellulose
P phosphorus
PO_x phosphorus oxides

■ REFERENCES

(1) Bing, R. G.; Sulis, D. B.; Carey, M. J.; Manesh, M. J. H.; Ford, K. C.; Straub, C. T.; Laemthong, T.; Alexander, B. H.; Willard, D. J.; Jiang, X.; Yang, C.; Wang, J. P.; Adams, M. W. W.; Kelly, R. M. Beyond Low Lignin: Identifying the Primary Barrier to Plant Biomass Conversion by Fermentative Bacteria. *Sci. Adv.* **2024**, *10* (42), No. eadq4941.

(2) Liang, J.; Xie, J.; Jiang, J.; Ma, Y.; Ye, J.; Zeng, X.; Wang, K. Environmentally Benign Process for Valorization of Lignocellulosic Bamboo Residues with Green Solvent Propylene Carbonate. *Green Energy Environ.* **2025**, *10*, 1777.

(3) Li, P.; Qian, W.; Wu, S.; Liu, Y. Acidic Deep Eutectic Solvents for Lignocellulose Pretreatment: Insights into Lignin Extraction Efficiency and Structural Transformation. *ACS Sustainable Chem. Eng.* **2025**, *13* (26), 9987−10018.

(4) Bosch, S. V. D.; Schutyser, W.; Vanholme, R.; Driessen, T.; Koelewijn, S.-F.; Renders, T.; Meester, B. D.; Huijgen, W. J. J.; Dehaen, W.; Courtin, C. M.; et al. Reductive Lignocellulose Fractionation into Soluble Lignin-Derived Phenolic Monomers and Dimers and Processable Carbohydrate Pulps. *Energy Environ. Sci.* **2015**, *8* (6), 1748−1763.

(5) Zhu, J. Y.; Pan, X. Efficient Sugar Production from Plant Biomass: Current Status, Challenges, and Future Directions. *Renew. Sust. Energy. Rev.* **2022**, *164*, 112583.

(6) Cheng, J.; Huang, C.; Zhan, Y.; Liu, X.; Wang, J.; Huang, C.; Fang, G.; Ragauskas, A. J.; Xie, Z.; Meng, X. A Novel Mineral-Acid Free Biphasic Deep Eutectic Solvent/γ-Valerolactone System for Furfural Production and Boosting the Enzymatic Hydrolysis of Lignocellulosic Biomass. *Bioresour. Technol.* **2023**, *387*, 129653.

(7) Reis, C. E. R.; Libardi Junior, N.; Bento, H. B. S.; Carvalho, A. K. F. D.; Vandenberghe, L. P. D. S.; Soccol, C. R.; Aminabhavi, T. M.; Chandel, A. K. Process Strategies to Reduce Cellulase Enzyme Loading for Renewable Sugar Production in Biorefineries. *Chem. Eng. J.* **2023**, *451*, 138690.

(8) Huang, C.; Jiang, X.; Shen, X.; Hu, J.; Tang, W.; Wu, X.; Ragauskas, A.; Jameel, H.; Meng, X.; Yong, Q. Lignin-Enzyme Interaction: A Roadblock for Efficient Enzymatic Hydrolysis of Lignocellulosics. *Renew. Sust. Energy. Rev.* **2022**, *154*, 111822.

(9) Ma, S.; Shiva; Tao, H.; Dempsey, J.; Chen, X.; Yuan, J.; Zhu, J. Y.; Yuan, J. S.; Zhou, L.; Yang, B. A Chemical-Recovery-Free Ammonium Sulfite-Based Alkali Pretreatment of Corn Stover for Low-Cost Sugar Production via Fertilizer Use of Waste Liquor. *Bioresour. Technol.* **2025**, *427*, 132402.

(10) Negahdar, L.; Delidovich, I.; Palkovits, R. Aqueous-Phase Hydrolysis of Cellulose and Hemicelluloses over Molecular Acidic Catalysts: Insights into the Kinetics and Reaction Mechanism. *Appl. Catal. B Environ.* **2016**, *184*, 285−298.

(11) Zhou, Z.; Liu, D.; Zhao, X. Conversion of Lignocellulose to Biofuels and Chemicals via Sugar Platform: An Updated Review on Chemistry and Mechanisms of Acid Hydrolysis of Lignocellulose. *Renew. Sust. Energy. Rev.* **2021**, *146*, 111169.

(12) Balasubramanian, S.; Shanmugam, R.; Basha, A. C.; Sriariyanun, M.; Shanmugam, S. R.; Venkatachalam, P. An Overview of Solid Acid Catalysts in Lignocellulose Biorefineries. *Catalysts* **2025**, *15* (5), 432.

(13) Xiong, S.; Guan, Y.; Luo, C.; Zhu, L.; Wang, S. Critical Review on the Preparation of Platform Compounds from Biomass or Saccharides via Hydrothermal Conversion over Carbon-Based Solid Acid Catalysts. *Energy Fuels* **2021**, *35* (18), 14462−14483.

(14) Lai, D.; Deng, L.; Guo, Q.; Fu, Y. Hydrolysis of Biomass by Magnetic Solid Acid. *Energy Environ. Sci.* **2011**, *4* (9), 3552−3557.

(15) Su, T.; Zeng, J.; Gao, H.; Jiang, L.; Bai, X.; Zhou, H.; Xu, F. One-Pot Synthesis of a Chemically Functional Magnetic Carbonaceous Acid Catalyst for Fermentable Sugars Production from Sugarcane Bagasse. *Fuel* **2020**, *262*, 116512.

(16) Qi, W.; Liu, G.; He, C.; Liu, S.; Lu, S.; Yue, J.; Wang, Q.; Wang, Z.; Yuan, Z.; Hu, J. An Efficient Magnetic Carbon-Based Solid Acid Treatment for Corncob Saccharification with High Selectivity for Xylose and Enhanced Enzymatic Digestibility. *Green Chem.* **2019**, *21* (6), 1292−1304.

(17) Cao, L.; Yu, I. K. M.; Tsang, D. C. W.; Zhang, S.; Ok, Y. S.; Kwon, E. E.; Song, H.; Poon, C. S. Phosphoric Acid-Activated Wood Biochar for Catalytic Conversion of Starch-Rich Food Waste into Glucose and 5-Hydroxymethylfurfural. *Bioresour. Technol.* **2018**, *267*, 242−248.

(18) Jung, H.; Yang, J.; Maeng, J.; Kim, W. B.; Yun, Y. Ammonia Production via Electrocatalytic Nitrate Reduction on Phosphorus-Doped Coconut Shell-Based Activated Carbons. *Appl. Surf. Sci.* **2025**, *686*, 162089.

(19) Zhou, X.; Liu, X.; Qi, F.; Shi, H.; Zhang, Y.; Ma, P. Efficient Preparation of P-Doped Carbon with Ultra-High Mesoporous Ratio from Furfural Residue for Dye Removal. *Sep. Purif. Technol.* **2022**, *292*, 120954.

(20) Qin, Y.; Ou, Z.; Guo, C.; Liu, Y.; Jin, R.; Xu, C.; Chen, H.; Si, Y.; Li, H. Phosphor-Doping Modulates the *d*-Band Center of Fe Atoms in Fe-N4 Catalytic Sites to Boost the Activity of Oxygen Reduction. *Appl. Catal. B Environ.* **2025**, *360*, 124553.

(21) Perdew, J. P.; Burke, K.; Ernzerhof, M. Generalized Gradient Approximation Made Simple. *Phys. Rev. Lett.* **1996**, *77* (18), 3865−3868.

(22) Dolg, M.; Wedig, U.; Stoll, H.; Preuss, H. Energy-adjustedab Initio Pseudopotentials for the First Row Transition Elements. *J. Chem. Phys.* **1987**, *86* (2), 866−872.

(23) Suganuma, S.; Nakajima, K.; Kitano, M.; Yamaguchi, D.; Kato, H.; Hayashi, S.; Hara, M. Hydrolysis of Cellulose by Amorphous Carbon Bearing SO_3H, COOH, and OH Groups. *J. Am. Chem. Soc.* **2008**, *130* (38), 12787−12793.

(24) Luo, Y.; Li, R.; Sun, X.; Liu, X.; Li, D. The Roles of Phosphorus Species Formed in Activated Biochar from Rice Husk in the Treatment of Landfill Leachate. *Bioresour. Technol.* **2019**, *288*, 121533.
(25) Li, Y.; Zhang, X.; Yang, R.; Li, G.; Hu, C. The Role of H_3PO_4 in the Preparation of Activated Carbon from NaOH-Treated Rice Husk Residue. *RSC Adv.* **2015**, *5* (41), 32626−32636.
(26) Jakob, A.; Likozar, B.; Grilc, M. Model-Assisted Optimization of Xylose, Arabinose, Glucose, Mannose, Galactose and Real Hemicellulose Streams Dehydration To (Hydroxymethyl)Furfural and Levulinic Acid. *ChemSuschem* **2024**, *17* (24), No. e202400962.
(27) Li, Z.; Jiang, Z.; Luo, Y.; Ge, C.; Wang, X.; Hu, C. Study on the Role of Alkali Halides on the Mutarotation and Dehydration of D-Xylose in Aqueous Solution. *Carbohydr. Res.* **2024**, *545*, 109258.
(28) Burhenne, L.; Messmer, J.; Aicher, T.; Laborie, M.-P. The Effect of the Biomass Components Lignin, Cellulose and Hemicellulose on TGA and Fixed Bed Pyrolysis. *J. Anal. Appl. Pyrolysis.* **2013**, *101*, 177−184.
(29) Questell-Santiago, Y. M.; Zambrano-Varela, R.; Talebi Amiri, M.; Luterbacher, J. S. Carbohydrate Stabilization Extends the Kinetic Limits of Chemical Polysaccharide Depolymerization. *Nat. Chem.* **2018**, *10* (12), 1222−1228.
(30) Sharma, R.; Selvaraj, T.; Gowri, V.; Devi, B.; Elumalai, S.; John Varghese, J.; Jayamurugan, G. Agri-Waste-Derived Phosphorylated Sporopollenin Catalyst Facilitates the Selective 5-Hydroxymethylfurfural Formation in Water: Insights into Phosphate Functionalization, and Mechanism. *ACS Sustainable Chem. Eng.* **2025**, *13* (25), 9455−9466.
(31) Dai, X.; Yan, P.; Bai, Y.; Guo, M.; Qi, W. Phosphorus modified onion-like carbon catalyzed methanol conversion to dimethoxymethane: The unique role of C−P species. *Carbon Future* **2024**, *1* (2), 9200012.
(32) Yin, Z.; Liu, X.; Wu, F.; Lu, B.; Huang, B.; Chen, Y.; Lin, G. Fabrication of P-Doped Porous Carbon Catalysts, with Inherent N Functionality, from Waste Peanut Shells and Their Application in the Metal-Free Aerobic Oxidation of Alcohols. *ACS Sustainable Chem. Eng.* **2022**, *10* (2), 911−922.
(33) Patel, M. A.; Luo, F.; Khoshi, M. R.; Rabie, E.; Zhang, Q.; Flach, C. R.; Mendelsohn, R.; Garfunkel, E.; Szostak, M.; He, H. P-Doped Porous Carbon as Metal Free Catalysts for Selective Aerobic Oxidation with an Unexpected Mechanism. *ACS Nano* **2016**, *10* (2), 2305−2315.
(34) Xiong, S.; Luo, C.; Yu, Z.; Ji, N.; Zhu, L.; Wang, S. Dual-Functional Carbon-Based Solid Acid-Induced Hydrothermal Conversion of Biomass Saccharides: Catalyst Rational Design and Kinetic Analysis. *Green Chem.* **2021**, *23* (21), 8458−8467.
(35) Robinson, I.; Tung, L. D.; Maenosono, S.; Wälti, C.; Thanh, N. T. K. Synthesis of Core-Shell Gold Coated Magnetic Nanoparticles and Their Interaction with Thiolated DNA. *Nanoscale* **2010**, *2* (12), 2624−2630.
(36) Liu, Z.; Peng, F.; Wang, H.; Yu, H.; Zheng, W.; Yang, J. Phosphorus-Doped Graphite Layers with High Electrocatalytic Activity for the O_2 Reduction in an Alkaline Medium. *Angew. Chem. Int. Ed.* **2011**, *50* (14), 3257−3261.
(37) Zhang, C.; Mahmood, N.; Yin, H.; Liu, F.; Hou, Y. Synthesis of Phosphorus-Doped Graphene and Its Multifunctional Applications for Oxygen Reduction Reaction and Lithium Ion Batteries. *Adv. Mater.* **2013**, *25* (35), 4932−4937.
(38) Li, J.; Zhang, Z.; Cui, M.; Liu, Q.; Fei, Z.; Chen, X.; Tang, J.; Qiao, X. Selective Addition of Isobutene over $ZrSiO_4/SiO_2$-SO_3H: Hydroacetoxylation versus Dimerization. *Catal.Commun.* **2021**, *148*, 106172.
(39) Ahangaran, F.; Hassanzadeh, A.; Nouri, S. Surface Modification of Fe3O4@SiO2Microsphere by Silane Coupling Agent. *Int. Nano Lett.* **2013**, *3* (1), 23.
(40) Liou, T.-H.; Wu, S.-J. Characteristics of Microporous/Mesoporous Carbons Prepared from Rice Husk under Base- and Acid-Treated Conditions. *J. Hazard. Mater.* **2009**, *171* (1), 693−703.
(41) Chen, H.; Yang, X.; Liu, Y.; Lin, X.; Wang, J.; Zhang, Z.; Li, N.; Li, Y.; Zhang, Y. KOH Modification Effectively Enhances the Cd and Pb Adsorption Performance of N-Enriched Biochar Derived from Waste Chicken Feathers. *Waste Management* **2021**, *130*, 82−92.
(42) Chen, C. W.; Huang, C. C.; Lin, Y. Y.; Chen, L. C.; Chen, K. H. The Affinity of Si−N and Si−C Bonding in Amorphous Silicon Carbon Nitride (a-SiCN) Thin Film. *Diam. Relat. Mater.* **2005**, *14* (3), 1126−1130.
(43) Lukose, R.; Lisker, M.; Akhtar, F.; Fraschke, M.; Grabolla, T.; Mai, A.; Lukosius, M. Influence of Plasma Treatment on SiO_2/Si and Si_3N_4/Si Substrates for Large-Scale Transfer of Graphene. *Sci. Rep.* **2021**, *11* (1), 13111.
(44) Zhang, J.; Liu, X.; Blume, R.; Zhang, A.; Schlögl, R.; Su, D. S. Surface-Modified Carbon Nanotubes Catalyze Oxidative Dehydrogenation of n-Butane. *Science* **2008**, *322* (5898), 73−77.
(45) Cao, X.; Zhao, J.; Long, F.; Zhang, X.; Xu, J.; Jiang, J. Al-Modified Pd@mSiO2 Core-Shell Catalysts for the Selective Hydrodeoxygenation of Fatty Acid Esters: Influence of Catalyst Structure and Al Atoms Incorporation. *Appl. Catal. B Environ.* **2022**, *305*, 121068.
(46) Lv, M.; Zhang, Y.; Xin, Q.; Yin, D.; Yu, S.; Liu, S.; Li, L.; Xie, C.; Wu, Q.; Yu, H.; Liu, Y. Pd@Al-Containing Mesoporous Silica Yolk−Shell-Structured Nanospheres as High Performance Nanoreactors for the Selective Hydrogenolysis of Glucose to 1,2-Propylene Glycol. *Chem. Eng. J.* **2020**, *396*, 125274.
(47) Luo, Y.; Li, D.; Chen, Y.; Sun, X.; Cao, Q.; Liu, X. The Performance of Phosphoric Acid in the Preparation of Activated Carbon-Containing Phosphorus Species from Rice Husk Residue. *J. Mater. Sci.* **2019**, *54* (6), 5008−5021.
(48) Fan, M.; Shao, Y.; Wang, Y.; Sun, J.; He, H.; Guo, Y.; Zhang, S.; Wang, S.; Li, B.; Hu, X. Evolution of Pore Structure and Functionalities of Activated Carbon and Phosphorous Species in Activation of Cellulose with H_3PO_4. *Renew. Energy* **2025**, *240*, 122151.
(49) Baghel, R. S.; Suthar, P.; Gajaria, T. K.; Bhattacharya, S.; Anil, A.; Reddy, C. R. K. Seaweed Biorefinery: A Sustainable Process for Valorising the Biomass of Brown Seaweed. *J. Clean. Prod.* **2020**, *263*, 121359.

https://doi.org/10.1021/acssuschemeng.5c11136
ACS Sustainable Chem. Eng. XXXX, XXX, XXX−XXX